In order to test whether this superhydrophobicity was kept after abrasion on the whole area but not merely on some points (contact angle measuring points), water droplet was guided by a needle to travel on the PDT glass surface after the 11th, 20th, 30th, and 40th cycle's abrasion, respectively (movie S12). The water droplet traveling after the 40th cycle is shown in Fig. 4D.

To enlarge the application scale and broaden the types of substrates, the spray adhesive [EVO-STIK (Bostik, UK)] was also used to bond glass, steel, cotton wool, and filter paper substrates with the superhydrophobic paint. We show in fig. S10 and movie S13 the finger-wipe tests on untreated, paint-treated, and "paint + spray adhesive"–treated (PSAT) substrates, respectively. On hard substrates (glass and steel), PSAT surfaces retained water proofing, whereas the paint was just removed when directly applied; the case is different on soft substrates (cotton and paper), on which paint was protected by their porous structures, resulting in both paint-treated and PSAT cotton and paper being superhydrophobic after the finger-wipe. However, in a more powerful test (sandpaper abrasion of cotton), this "protection" is limited (fig. S11). As shown in fig. S12 and movie S14, the sandpaper abrasion tests on PSAT substrates and both hard and soft substrates became robust after the PSAT treatment. As shown in fig. S13 and movie S15, the PSAT substrates retained water repellency after knife-scratch tests. After different damages, the PSAT materials still remained superhydrophobic, indicating that this method could efficiently enhance the robustness of superhydrophobic surfaces on different substrates; it is believed that the idea of "superhydrophobic paint + adhesives" can be simply, flexibly, and robustly used in large-scale industrial applications.

The superhydrophobic surfaces show that a robust resistance to oil contamination and ease of applicability can be achieved by implementing straightforward coating methods such as spraying, dip-coating, or even simply extrusion from a syringe. The flexibility of the "paint + adhesives" combination enables both hard and soft substrates to become robustly superhydrophobic and self-cleaning. The surfaces can be readily implemented in harsh and oily environments where robustness is required.

REFERENCES AND NOTES

1. W. Barthlott, C. Neinhuis, *Planta* **202**, 1–8 (1997).
2. R. Blossey, *Nat. Mater.* **2**, 301–306 (2003).
3. I. P. Parkin, R. G. Palgrave, *J. Mater. Chem.* **15**, 1689 (2005).
4. T. Onda, S. Shibuichi, N. Satoh, K. Tsujii, *Langmuir* **12**, 2125–2127 (1996).
5. L. Feng *et al.*, *Adv. Mater.* **14**, 1857–1860 (2002).
6. J. Zimmermann, F. A. Reifler, G. Fortunato, L. C. Gerhardt, S. Seeger, *Adv. Funct. Mater.* **18**, 3662–3669 (2008).
7. X. Zhu *et al.*, *J. Mater. Chem.* **21**, 15793 (2011).
8. Q. Zhu *et al.*, *J. Mater. Chem. A* **1**, 5386 (2013).
9. A. Tuteja *et al.*, *Science* **318**, 1618–1622 (2007).
10. X. Deng, L. Mammen, H. J. Butt, D. Vollmer, *Science* **335**, 67–70 (2012).
11. Y. Lu *et al.*, *ACS Sustainable Chem. Eng.* **1**, 102 (2013).
12. Materials and methods are available as supplementary materials on *Science* Online.
13. D. Richard, C. Clanet, D. Quéré, *Nature* **417**, 811 (2002).
14. J. C. Bird, R. Dhiman, H. M. Kwon, K. K. Varanasi, *Nature* **503**, 385–388 (2013).
15. Y. Lu *et al.*, *J. Mater. Chem. A* **2**, 12177 (2014).
16. D. Vella, L. Mahadevan, *Am. J. Phys.* **73**, 817 (2005).
17. A. Tuteja, W. Choi, J. M. Mabry, G. H. McKinley, R. E. Cohen, *Proc. Natl. Acad. Sci. U.S.A.* **105**, 18200–18205 (2008).
18. A. Nakajima *et al.*, *Langmuir* **16**, 7044–7047 (2000).
19. R. Fürstner, W. Barthlott, C. Neinhuis, P. Walzel, *Langmuir* **21**, 956–961 (2005).
20. B. Bhushan, Y. C. Jung, K. Koch, *Langmuir* **25**, 3240–3248 (2009).
21. T. S. Wong *et al.*, *Nature* **477**, 443–447 (2011).
22. M. Nosonovsky, *Nature* **477**, 412–413 (2011).
23. A. Grinthal, J. Aizenberg, *Chem. Mater.* **26**, 698–708 (2014).
24. D. C. Leslie *et al.*, *Nat. Biotechnol.* **32**, 1134–1140 (2014).
25. M. Im, H. Im, J. Lee, J. Yoon, Y. Choi, *Soft Matter* **6**, 1401 (2010).
26. B. Wang *et al.*, *ACS Appl. Mater. Interfaces* **5**, 1827–1839 (2013).

ACKNOWLEDGMENTS

We thank M. Vickers and S. Firth for XRD and TEM characterizations. Thanks to C. E. Knapp and D. S. Bhachu for ordering chemicals and the help with some experiments.

SUPPLEMENTARY MATERIALS

www.sciencemag.org/content/347/6226/1132/suppl/DC1
Materials and Methods
Supplementary Text
Figs. S1 to S13
References (*27*, *28*)
Movies S1 to S15

16 October 2014; accepted 30 January 2015
10.1126/science.aaa0946

PROTEIN IMAGING

Single-protein spin resonance spectroscopy under ambient conditions

Fazhan Shi,[1,2,3]* Qi Zhang,[1,2]* Pengfei Wang,[1,2,3]* Hongbin Sun,[4] Jiarong Wang,[4] Xing Rong,[1,2,3] Ming Chen,[1,2] Chenyong Ju,[1,2,3] Friedemann Reinhard,[5]† Hongwei Chen,[4] Jörg Wrachtrup,[5] Junfeng Wang,[4] Jiangfeng Du[1,2,3]‡

Magnetic resonance is essential in revealing the structure and dynamics of biomolecules. However, measuring the magnetic resonance spectrum of single biomolecules has remained an elusive goal. We demonstrate the detection of the electron spin resonance signal from a single spin-labeled protein under ambient conditions. As a sensor, we use a single nitrogen vacancy center in bulk diamond in close proximity to the protein. We measure the orientation of the spin label at the protein and detect the impact of protein motion on the spin label dynamics. In addition, we coherently drive the spin at the protein, which is a prerequisite for studies involving polarization of nuclear spins of the protein or detailed structure analysis of the protein itself.

Observing the structure and dynamics of single molecules is a long-sought goal that has inspired technical developments in a wide range of disciplines (*1*–*4*). As one of the most important techniques, electron spin resonance (ESR) finds broad application for studying basic molecular mechanisms in biology and chemistry (*5*). Most proteins, however, are nonparamagnetic and thus cannot be accessed by the technique. Labeling biomolecules with a small spin-bearing moiety, such as nitroxide spin labels, enables ESR to acquire a broad range of structural and dynamical information. However, current methods need 10^{10} uniform molecules to accumulate a large enough signal-to-noise ratio. This substantially complicates efforts to compile structural and dynamical information. New methods that have tried to push the sensitivity of magnetic resonance to the single-spin level all require either a dedicated environment (*6*, *7*) or conducting surfaces and tips (*8*).

A sensor that could accomplish single-protein detection under ambient conditions is a recently developed atomic-sized magnetic field sensor based on the nitrogen vacancy (NV) defect center in diamond (*9*–*11*). Because of its long coherence times (*12*, *13*), the NV sensor can detect a single electron spin over a distance of 30 nm under ambient conditions. As proof-of-principle demonstrations, single electron spins inside diamond or on diamond surfaces have been sensed (*14*–*16*). Despite previous efforts, single-biomolecule detection and spectroscopy have not been attained. Here, we report an electron spin resonance study on a single protein, which allows us to extract the structural and dynamical properties from spectral analysis.

As the experimental sample, we chose MAD2 (mitotic arrest deficient-2), an essential spindle

[1]Hefei National Laboratory for Physical Sciences at the Microscale and Department of Modern Physics, University of Science and Technology of China (USTC), Hefei 230026, China. [2]Joint Laboratory of Quantum Biophysics, USTC Institute of Biophysics and Chinese Academy of Sciences. [3]Synergetic Innovation Center of Quantum Information and Quantum Physics, USTC, Hefei 230026, China. [4]High Magnetic Field Laboratory, Chinese Academy of Sciences, Hefei 230000, China. [5]3rd Physics and Integrated Quantum Science and Technology (IQST), University of Stuttgart, 70569 Stuttgart, Germany.
*These authors contributed equally to this work. †Present address: Walter Schottky Institut, E24, Technische Universität München, 85748 Garching, Germany. ‡Corresponding author. E-mail: djf@ustc.edu.cn

checkpoint protein (*17*, *18*). The spindle checkpoint is a major cell cycle control mechanism that prevents errors in chromosome segregation and aneuploidy, thereby ensuring the fidelity of chromosome inheritance. We chose this protein for the present study because it can be easily modified site-specifically with a single nitroxide spin label. In addition, it is reliably immobilized on the diamond surface by embedding it in a polylysine layer. We detected this spin label by its magnetic dipole interaction with a single NV center (*19*). In brief, the NV center consists of a nitrogen impurity and a neighboring vacancy. Its triplet (S = 1) ground state can be spin-polarized and read out optically. The magnetic dipole interaction between the NV spin and the spin label is conveniently measured by simultaneously driving the probe (NV) and the sample spin (spin label) (*20*). Single NV centers were created roughly 5 nm below the surface of diamond by ion implantation (*21*). We did not position MAD2 with respect to single NV centers in a controlled way, so our experiments rely on statistical proximity. For this purpose, the protein surface concentration was optimized by atomic force microscopy (AFM) (Fig. 1B and fig. S1) and various NV centers were tested for dipolar interaction with single spin labels (fig. S2).

Detecting the single-electron spin label is challenging because the coherence time of shallow NV centers is usually limited by surface noise, which obscures the coupling between the spin label and the NV center. The spin label electron spin can be reliably detected by combining the spin resonance of the NV and the spin label with dynamical decoupling. The experimental pulse sequences are shown in Fig. 1C. Periodic XY8-N pulses on the NV sensor were used to preserve the NV sensor coherence and to increase its magnetic field sensitivity; radio-frequency (RF) pulses on the nitroxide spin labels were used to flip the electron spin synchronously.

Denoting the spins by S_{NV} (NV sensor), S_e (electron spin of nitroxide spin labels), and I (nitrogen nuclear spin of spin labels), the combined system can be modeled by a coupling Hamiltonian:

$$H = \overbrace{\Delta S_{z,NV}^2 + \gamma_{NV} B_0 S_{z,NV}}^{H_{NV}} + \overbrace{b S_{z,NV} S_{z,e}}^{H_{NV,SL}} + \overbrace{\gamma_e B_0 S_{z,e} + S_e A I + \gamma_I B_0 I_z + I Q I}^{H_{SL}} \quad (1)$$

where SL denotes the spin label, B_0 is the external static field (aligned along z), Δ is the zero-field splitting of the NV, Q is the nuclear quadrupole coupling constant, and γ_{NV}, γ_e, and γ_I are the gyromagnetic ratios of the NV, target electron, and nuclear spin, respectively. The coupling between the NV and the spin label is approximated as a pure $S_{z,NV}$–$S_{z,e}$ interaction with coupling constant b because it is much smaller than the Zeeman and zero-field splitting of the two spins. Within this approximation, the target spin generates an effective magnetic field $B_e = bS_{z,e}/\gamma_{NV}$ at the NV center site, which depends on the quantum number $S_{z,e}$.

We addressed the effective two-level system $|0\rangle = |S_{z,NV} = 0\rangle$; $|1\rangle = |S_{z,NV} = 1\rangle$ of the NV sensor with resonant microwave pulses and performed a dynamic decoupling experiment on this system. In this measurement, an initial $\pi/2$ pulse prepared the sensor in a coherent superposition,

$$\psi(t = 0) = \frac{|0\rangle + \exp(i\varphi)|1\rangle}{\sqrt{2}} \quad (2)$$

with $\varphi(t = 0) = 0$. The phase φ evolved over time, was refocused by N π-pulses at $t = \tau_0/2 + n\tau_0$, and was converted into a population by the final $\pi/2$ pulse at $t = N\tau_0$. The key idea of the experiment is to map the electron spin resonance signal of the spin label S_e to a phase φ on the NV spin. This goal was accomplished by manipulation of the electron spin on the protein (Fig. 1C, "spin label") synchronized with the dynamical decoupling period. The NV experienced an alternating field from the protein spin label and acquired a phase

$$\varphi \sim b_{eff} N \tau_0 \quad (3)$$

where b_{eff} is the effective magnetic field generated by the spin label at the location of the NV spin. In this way, the protein spin ESR signal is mapped to the signal obtained from the NV sensor.

Figure 2A shows the ESR spectrum of a single spin label. Upon cleaning the diamond surface, the signal disappeared, hence it stemmed from the spin label on the protein. The spectra in Fig. 2A were recorded at an external magnetic field B_0 = 153.0 G. Three spectral peaks at 356.3, 430.9, and 501.6 MHz mark the hyperfine splitting between the spin label electron spin (S = ½) and the nitrogen nuclear spin I = 1, similar to the ensemble results in Fig. 2B. The observation of hyperfine splitting proves that the detected spin is indeed the nitroxide spin on the protein and not, for instance, that of a substitutional nitrogen impurity inside diamond. Spectra from single

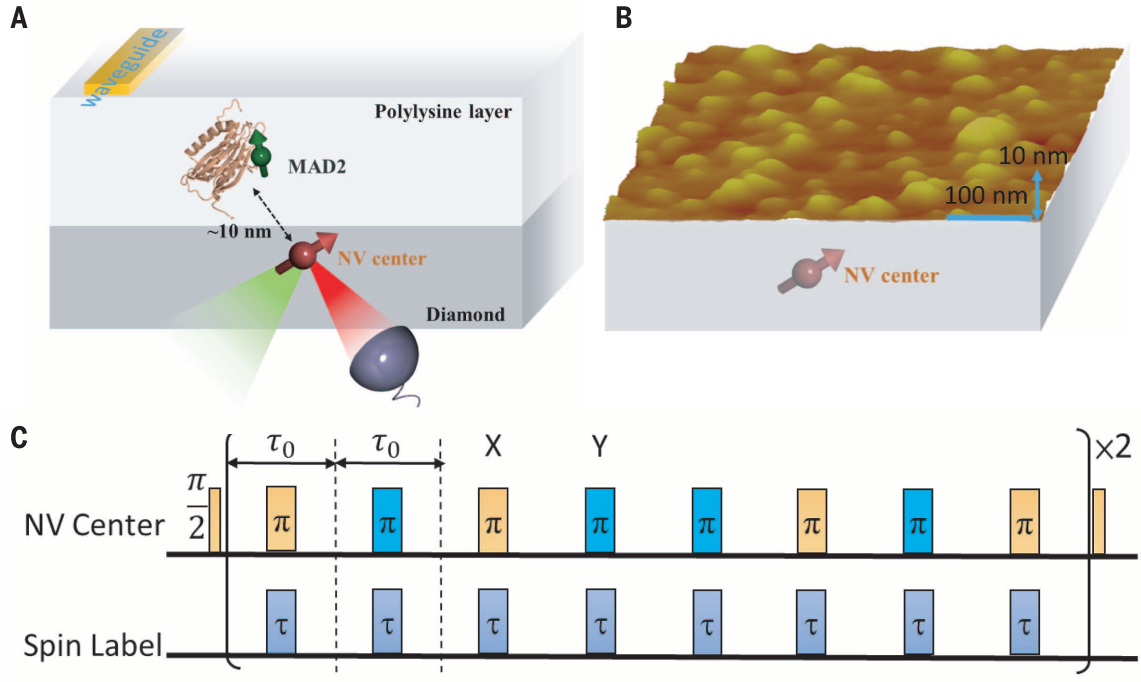

Fig. 1. Schematic of the setup and experimental method. (**A**) MAD2 proteins labeled with nitroxide spin labels, located on the surface of diamond, close to which NV centers were implanted. Microwaves were applied by a coplanar waveguide. (**B**) Distribution of freeze-dried proteins on the diamond surface measured by AFM. (**C**) Pulse sequence to measure the coupling of an NV sensor to the protein. The pulse sequence contains MW and RF channels, in which microwave and radio-frequency pulses were used to control the NV probe and synchronously flip the spin label (i.e., the nitroxide electron spin).

electron spins were markedly different from those measured on ensembles (*22*) (Fig. 2B). The ensemble ESR spectrum recorded on spin labels in fluid solution shows a spectrum with three equidistantly spaced peaks (Fig. 2B, upper panel). Here, fast tumbling of molecules averages out the anisotropic terms of the hyperfine interaction. Overall, the spectrum of a single spin label is closer to a solid-state spin ensemble (Fig. 2B, lower panel). However, for the solid-state ensemble spectrum, the random orientation of the molecular spin principal axis causes broadening of spectral peaks (*23*) (Fig. 2B, lower panel) and marked side shoulders. The spectra of the single molecule, however, show three clearly resolved peaks. Figure 2 underpins one benefit of single spin ESR: The anisotropic hyperfine coupling can be determined reliably. This is important for structural and dynamical information, as shown below.

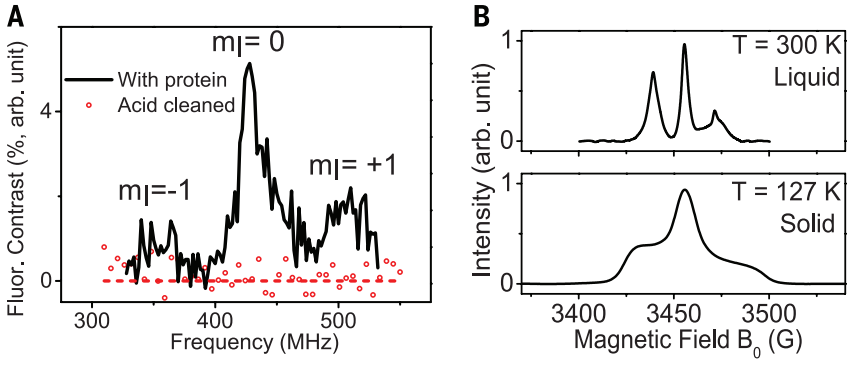

Fig. 2. Electron spin resonance spectrum of nitroxide spin labels. (**A**) Single spin ESR spectra under ambient conditions. The spectrum disappears after removing the protein by acid cleaning. (**B**) Upper curve: Ensemble ESR spectrum of ~10^{16} protein molecules in buffer solution at room temperature. Lower curve: Ensemble ESR spectrum of protein molecules in a frozen buffer solution with glycerine at T = 127 K.

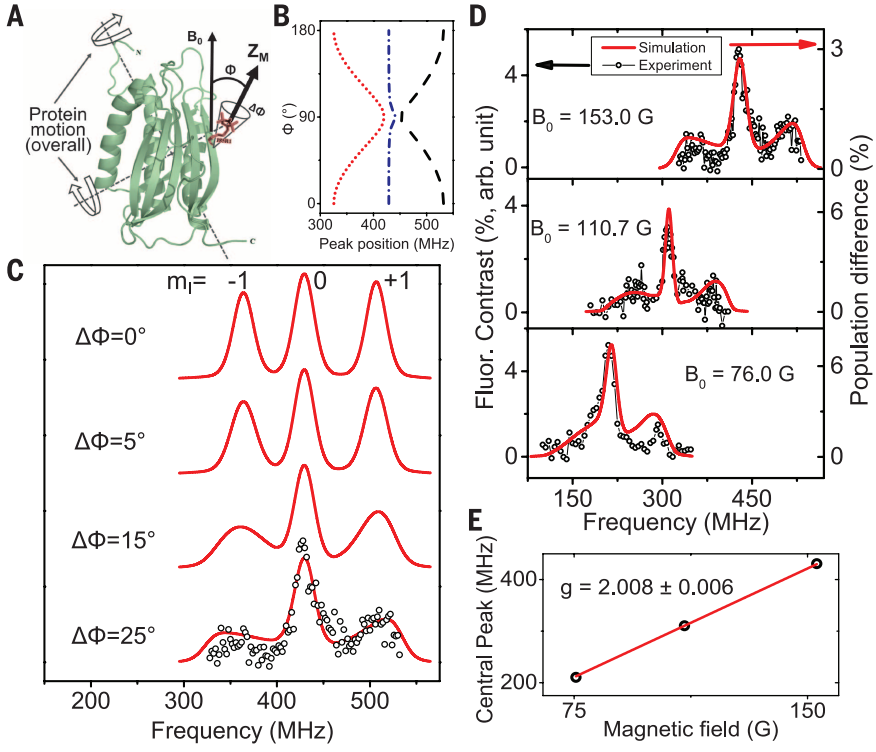

Fig. 3. Dynamics of the spin label. (**A**) Protein with spin label attached. $\mathbf{B}_0$ direction and spin label principal axis are shown. (**B**) Dependence of transition frequencies, corresponding to m_I = –1, 0, +1 transitions, on the angle Φ (between axis of spin label and external magnetic fields) and B_0 = 153 G. (**C**) Simulation of the single-protein ESR spectrum. The spectrum is best described by a tilt angle of the spin label Z_m axis of ⟨Φ⟩ = 46°. To describe broadening of m_I = –1, +1 components, a variation of ΔΦ = 25° was adopted. (**D**) ESR spectra of single spin labels at various external magnetic fields. All three peaks shifted with the magnetic field, and the middle peak evolved at the gyromagnetic ratio of a free electron spin. (**E**) Resonance frequency of the central peak in (D) as a function of external magnetic field, corresponding to a gyromagnetic ratio of 2.809 ± 0.011 MHz/G and a g-factor of 2.008.

The polylysine matrix used to immobilize MAD2 on the diamond surface restricts protein and spin label motion. However, neither protein nor spin label dynamics is fully frozen in these matrices. Indeed, molecular dynamics is revealed by a closer analysis of the spectra (Fig. 3). Depending on the size of the molecular part undergoing dynamics, its impact on the spectra is different. In the case that only the spin label is undergoing dynamics, its motion is expected to occur on a nanosecond time scale (*24*), which is not captured by our method. However, overall slow protein motion or dynamics occurs on a millisecond time scale (*21*, *25*). In our spectra, this shows up as broadening of spectral side peaks, which are indeed observed in our experiments (Fig. 3C). Without dynamics, one would expect three spectral lines for the three hyperfine levels of ^{14}N with identical intensity (Fig. 3C, upper trace). Motion specifically changing the direction of the nitrogen p orbitals (ZM in Fig. 3A) with respect to $\mathbf{B}_0$ causes a broadening of the $m_I = \pm 1$ peaks, as it modulates hyperfine splitting. Note that a rotation of the spin label around B_0 would not cause broadening and hence is not detected in our scheme.

To quantify protein motion, we performed a simulation of the ESR spectra using Eq. 1. The spectra are best described by a spin label, which shows a tilt angle of 46° with respect to $\mathbf{B}_0$. The spectral features could only be reproduced accurately by assuming that there is an additional motion around this tilt angle of ±25°. We attribute this motion to protein dynamics. The slight asymmetry of $m_I = \pm 1$ peaks, with splitting values 74.6 MHz and 70.7 MHz, is caused by the contribution of nonsecular hyperfine terms at low field. Upon reduction of the external magnetic field, the asymmetry became even more obvious (Fig. 3D, lower panel; see also table S2). The red curves in Fig. 3D are simulations using the Hamiltonian of Eq. 1, yielding an electron Zeeman factor (g-factor) of the spin label of 2.008, in good agreement with reported values (Fig. 3E).

Surprisingly, the dephasing and relaxation time of the spin label at the protein, even under ambient conditions, were long enough to generate and measure spin coherence, as shown by the Rabi oscillation of the spin label in Fig. 4A. We recorded the traces by fixing the RF frequency on the central peak of the spin label spectrum and varying the pulse duration time τ (Fig. 1C). The nutation frequency in Fig. 4A scaled with power, as expected from the Rabi oscillations (fig. S4). The method further allows us to determine the distance between the spin label and the NV probe. In Eq. 3, the phase acquired by the NV spin through the dipolar interaction with the spin label φ is proportional to $b_{eff}N\tau_0$. Because b_{eff} scales as d^{-3}, where d is the distance between the spin label and the NV spin, measuring the evolution of the phase thus allowed us to determine d. From a simulation of the curve in Fig. 4B, we derived a coupling strength of 90 kHz. This corresponds to $d \approx 9$ nm, with precise value depending on the orientation of the vector from the NV center to the spin label (fig. S6).

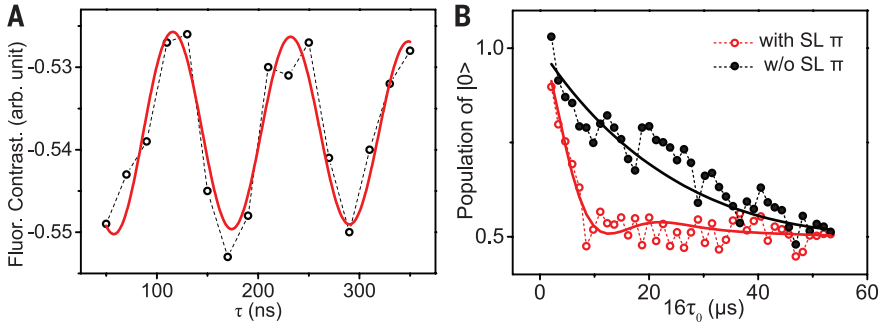

Fig. 4. Coherence and relaxation of protein spin. (**A**) Rabi oscillation of single spin label measured by using the sequence in Fig. 1B (fixing τ_0 and RF frequency at middle peak, varying τ). The solid curve is a fit using a sine function with exponential damping. (**B**) The red circles are measured by the double electron-electron resonance sequences on NV sensor and protein spin (fixing τ equal to spin label π pulse and RF frequency to the central peak, varying τ_0). The black dot is the NV center decoherence curve without protein spin flipping. The solid curves show the best simulation of both of the experimental results in (B), corresponding to a relaxation time of 4 μs for the spin label and 90 kHz coupling between spin label and NV center.

Relaxation of the protein electron spin is an important parameter to characterize the environment, including information on molecular dynamics. Here, we deduced the longitudinal relaxation time of the spin label from Fig. 4B. The red circles denote the interaction signal between the NV center and the spin label; the black dots show the NV center decoherence curve without operation on the spin label. Simulation (solid curves) shows a relaxation time of 4 μs. These values are compatible with those for spin labels in ensemble measurements, as the relaxation time of this kind of spin label is ~110 μs at liquid nitrogen temperature (*21*, *24*).

The ability to address single-electron spin labels on proteins adds another element to the emerging diamond sensor–based toolbox for ultraprecise structure determination. Together with the recently established nuclear magnetic resonance (NMR) detection, the present method extends the sensing range to dozens of nanometers, whereas diamond sensor–based NMR only senses nuclear spins in very close proximity (a few nanometers) to the NV center (*26*–*29*). The interaction between the spin label and the neighboring nuclei could be used to sense more distant nuclei and provide structural and dynamical information otherwise inaccessible by the sensor. In this respect, it is particularly encouraging that we find long spin relaxation times enabling coherent spin driving at the protein. This capability will allow the use of the ancillary electron spin for sophisticated coherent control (*30*, *31*), thereby facilitating future polarization transfer experiments that could gain access to nuclear spins in proteins, including proton or ^{13}C spins. When combined with either scanning magnetometry or nanoscale magnetic resonance imaging based on magnetic field gradients, protein structure analysis under ambient conditions at the level of a single molecule is within reach (*32*, *33*).

.

REFERENCES AND NOTES

1. L. Redecke *et al.*, *Science* **339**, 227–230 (2013).
2. T. R. M. Barends *et al.*, *Nature* **505**, 244–247 (2014).
3. M. C. Scott *et al.*, *Nature* **483**, 444–447 (2012).
4. C. C. Chen *et al.*, *Nature* **496**, 74–77 (2013).
5. P. P. Borbat, A. J. Costa-Filho, K. A. Earle, J. K. Moscicki, J. H. Freed, *Science* **291**, 266–269 (2001).
6. D. Rugar, R. Budakian, H. J. Mamin, B. W. Chui, *Nature* **430**, 329–332 (2004).
7. M. Xiao, I. Martin, E. Yablonovitch, H. W. Jiang, *Nature* **430**, 435–439 (2004).
8. Y. Manassen, R. J. Hamers, J. E. Demuth, A. J. Castellano Jr., *Phys. Rev. Lett.* **62**, 2531–2534 (1989).
9. G. Balasubramanian *et al.*, *Nature* **455**, 648–651 (2008).
10. J. R. Maze *et al.*, *Nature* **455**, 644–647 (2008).
11. J. M. Taylor *et al.*, *Nat. Phys.* **4**, 810–816 (2008).
12. G. Balasubramanian *et al.*, *Nat. Mater.* **8**, 383–387 (2009).
13. N. Bar-Gill, L. M. Pham, A. Jarmola, D. Budker, R. L. Walsworth, *Nat. Commun.* **4**, 1743 (2013).
14. M. S. Grinolds *et al.*, *Nat. Phys.* **9**, 215–219 (2013).
15. B. Grotz *et al.*, *New J. Phys.* **13**, 055004 (2011).
16. A. O. Sushkov *et al.*, *Nano Lett.* **14**, 6443–6448 (2014).
17. L. S. Michel *et al.*, *Nature* **409**, 355–359 (2001).
18. S. Martin-Lluesma, V. M. Stucke, E. A. Nigg, *Science* **297**, 2267–2270 (2002).
19. M. W. Doherty *et al.*, *Phys. Rep.* **528**, 1–45 (2013).
20. F. Z. Shi *et al.*, *Phys. Rev. B* **87**, 195414 (2013).
21. See supplementary materials on *Science* Online.
22. V. Gaponenko *et al.*, *Protein Sci.* **9**, 302–309 (2000).
23. J. A. Weil, J. R. Bolten, *Electron Paramagnetic Resonance: Elementary Theory and Practical Applications* (Wiley, New York, ed. 2, 2007), pp. 316–317.
24. K. Jacobsen, S. Oga, W. L. Hubbell, T. Risse, *Biophys. J.* **88**, 4351–4365 (2005).
25. M. A. Hemminga, L. J. Berliner, *ESR Spectroscopy in Membrane Biophysics* (Springer Science and Business Media, New York, 2007), pp. 133–134.
26. T. Staudacher *et al.*, *Science* **339**, 561–563 (2013).
27. H. J. Mamin *et al.*, *Science* **339**, 557–560 (2013).
28. F. Z. Shi *et al.*, *Nat. Phys.* **10**, 21–25 (2014).
29. C. Müller *et al.*, *Nat. Commun.* **5**, 4703 (2014).
30. M. Schaffry, E. M. Gauger, J. J. L. Morton, S. C. Benjamin, *Phys. Rev. Lett.* **107**, 207210 (2011).
31. A. O. Sushkov *et al.*, *Phys. Rev. Lett.* **113**, 197601 (2014).
32. M. S. Grinolds *et al.*, *Nat. Nanotechnol.* **9**, 279–284 (2014).
33. L. Luan *et al.*, http://arxiv.org/abs/1409.5418 (2014).

ACKNOWLEDGMENTS

We thank F. Jelezko for helpful discussions. Supported by 973 Program grants 2013CB921800 and 2012CB917202, National Natural Science Foundation of China grants 11227901, 91021005, 31470835, 11275183, and 21103199, and the Chinese Academy of Sciences. J.W. was supported by the Max Planck Society and the European Union (via the ERC grants SQUTEC and DIADEMS) and by the Baden-Württemberg Stiftung.

SUPPLEMENTARY MATERIALS

www.sciencemag.org/content/347/6226/1135/suppl/DC1
Materials and Methods
Tables S1 and S2
Figs. S1 to S7
References (*34*–*37*)

3 November 2014; accepted 29 January 2015
10.1126/science.aaa2253

BRAIN STRUCTURE

Cell types in the mouse cortex and hippocampus revealed by single-cell RNA-seq

Amit Zeisel,[1]* Ana B. Muñoz-Manchado,[1]* Simone Codeluppi,[1] Peter Lönnerberg,[1] Gioele La Manno,[1] Anna Juréus,[1] Sueli Marques,[1] Hermany Munguba,[1] Liqun He,[2] Christer Betsholtz,[2,3] Charlotte Rolny,[4] Gonçalo Castelo-Branco,[1] Jens Hjerling-Leffler,[1]† Sten Linnarsson[1]†

The mammalian cerebral cortex supports cognitive functions such as sensorimotor integration, memory, and social behaviors. Normal brain function relies on a diverse set of differentiated cell types, including neurons, glia, and vasculature. Here, we have used large-scale single-cell RNA sequencing (RNA-seq) to classify cells in the mouse somatosensory cortex and hippocampal CA1 region. We found 47 molecularly distinct subclasses, comprising all known major cell types in the cortex. We identified numerous marker genes, which allowed alignment with known cell types, morphology, and location. We found a layer I interneuron expressing *Pax6* and a distinct postmitotic oligodendrocyte subclass marked by *Itpr2*. Across the diversity of cortical cell types, transcription factors formed a complex, layered regulatory code, suggesting a mechanism for the maintenance of adult cell type identity.

The brain is built from a large number of specialized cell types, enabling highly refined electrophysiological behavior, as well as fulfilling brain nutrient needs and defense against pathogens. Functional specialization allows fine-tuning of circuit dynamics and decoupling of support functions such as energy supply, waste removal, and immune defense. Cells in the nervous system have historically been classified using location, morphology, target specificity, and

Single-protein spin resonance spectroscopy under ambient conditions

Fazhan Shi *et al.*

Science **347**, 1135 (2015);
DOI: 10.1126/science.aaa2253